

Revision 2

High-pressure single-crystal structural analysis of AlSiO₃OH Phase Egg

¹*Kirsten Schulze, ²Martha G. Pamato, ¹Alexander Kurnosov, ¹Tiziana Boffa Ballaran, ³Konstantin Glazyrin, ³Anna Pakhomova, ^{1,4}Hauke Marquardt

¹ Bayerisches Geoinstitut, University Bayreuth, 95440 Bayreuth, Germany

² Department of Earth Sciences, University College London, WC1E 6BT London, United Kingdom

³ FS-PE, Deutsches Elektronen Synchrotron, Hamburg, Germany

⁴ Department of Earth Sciences, University of Oxford, OX1 3AN Oxford, UK

* correspond to: Kirsten.Schulze@uni-bayreuth.de

Abstract

We present the first equation of state and structure refinements at high-pressure of single-crystal Phase Egg, AlSiO₃OH. Phase Egg is a member of the Al₂O₃-SiO₂-H₂O system, which contains phases that may be stable along a typical mantle geotherm (Fukuyama et al. 2017) and are good candidates for water transport into Earth's deep mantle. Single-crystal synchrotron X-ray diffraction was performed up to 23 GPa. We observe the **b** axis to be the most compressible direction and the β angle to decrease up to 16 GPa and then to remain constant at a value of $\sim 97.8^\circ$ up to the maximum experimental pressure. Structure refinements performed at low pressures reveal a distorted octahedron around the silicon atom due to one of the six Si-O bond lengths being significantly larger than the other five. The length of this specific Si-O4 bond rapidly decreases with increasing pressure leading to a more regular octahedron at pressures above 16 GPa. We identified the shortening of the Si-O4 bond and the contraction of the vacant space between octahedral units where the hydrogen atoms are assumed to lie as the major components of the compression mechanism of AlSiO₃OH Phase Egg.

26

INTRODUCTION

27 Hydrous aluminosilicate phases show a larger temperature stability field than the respective Mg-
28 endmembers and are expected to be stable along a typical geotherm (Fukuyama et al. 2017).
29 Therefore, they are assumed to play an important role in the Earth's deep water cycle (Gatta et al.
30 2014, Pamato et al. 2015, Fukuyama et al. 2017). AlSiO₃OH Phase Egg is stable within the
31 transition zone (Sano et al. 2004, Fukuyama et al. 2017) and probably also in the upper lower
32 mantle up to pressures of 26 GPa at 1460 – 1600 °C (Pamato et al. 2015). Nanocrystalline diamond
33 inclusions with a 1:1 Al to Si composition were found, providing direct indication for its existence
34 within Earth's mantle (Wirth et al. 2007). AlSiO₃OH Phase Egg was first synthesized by Eggleton
35 et al. (1978) and its structure was first solved by Schmidt et al. (1998). Phase Egg has a monoclinic
36 structure with $P2_1/n$ space group (Figure 1) and the ideal formula AlSiO₃OH contains 7.5 wt%
37 H₂O. The crystal structure is made up by columns of edge-shared octahedra corner linked to the
38 other columns with hydrogen occupying the vacant space between columns (Schmidt et al. 1998)
39 bonded to the O4 oxygen atoms. Vanpeteghem et al. (2003) performed a X-ray powder diffraction
40 study on Phase Egg to a maximum pressure of 40 GPa at room temperature and described its
41 compressibility using a third order Birch-Murnaghan equation of state with a room pressure bulk
42 modulus $K_0 = 157(4)$ GPa and its pressure-derivative $K_0' = 6.5(4)$. This previous study has
43 highlighted the anisotropic compression response of Phase Egg with the shortest unit-cell axis being
44 the most compressible. Vanpeteghem et al. (2003) suggested that this behavior may be caused by a
45 larger compression of some of the O-O distances, but they have not performed structural
46 refinements at high pressure to support this hypothesis.

47 Here, we present the first single-crystal X-ray diffraction data on Phase Egg collected to a
48 maximum pressure of 23 GPa at ambient temperature using neon as a pressure-transmitting
49 medium. Our single-crystal data allows for the characterisation of the structural evolution of Phase
50 Egg with pressure and the clear identification of the compression mechanisms.

51

52

METHODS

53 **Sample synthesis and characterization**

54 Phase Egg single-crystals were synthesized at 26 GPa and 1600 °C in a 1000 t Kawai type multi-
55 anvil apparatus at the Bayerisches Geoinstitut (BGI) (run number: S5050) using a mixture of
56 $\text{Al}_2\text{O}_3:\text{Al}(\text{OH})_3:\text{SiO}_2$ in a wt.% ratio of 13.59:39.27:47.15 as starting composition. The run product
57 resulted in a mixture of Phase Egg, Al-phase D and Stishovite. Further details on the synthesis and
58 characterization are given in Pamato et al. (2015). The chemical composition of Phase Egg as
59 determined by microprobe analysis by Pamato et al. (2015) is $\text{Al}_{0.98(1)}\text{Si}_{0.92(1)}\text{O}_3\text{OH}_{1.39(5)}$.

60 A single-crystal with dimensions 28 x 77 x 42 μm^3 that showed sharp diffraction profiles, with a
61 full width at half maximum in omega scans below 0.06°, was selected from the run product and
62 measured at ambient conditions on a four-circle Huber diffractometer equipped with $\text{MoK}\alpha$
63 radiation and a point detector at BGI. A total of 25 reflections between 15° and 40° in 2 θ were
64 centered using the eight-position centering method according to the procedure of King and Finger
65 (1979) implemented in the SINGLE operating software (Angel and Finger 2011). The unit-cell
66 lattice parameters were determined using vector-least-squares refinements (Table 1). Single-crystal
67 X-ray diffraction measurements for structure refinement at ambient conditions were performed at
68 BGI using an Oxford XCalibur diffractometer using $\text{MoK}\alpha$ radiation ($\lambda = 0.70937 \text{ \AA}$) operated at 50
69 kV and 40 mA. The system is equipped with a graphite monochromator and a Sapphire 2 CCD area
70 detector at a distance of 50.83 mm. Omega scans were chosen to obtain a large redundancy of the
71 reciprocal sphere up to $2\theta_{\text{max}} = 81^\circ$. Frames were collected for 10 seconds using a step size of 0.5°.
72 The CrysAlis package (Oxford Diffraction 2006) was used to integrate the intensity data taking into
73 account both Lorentz and polarization factors as well as an empirical absorption correction. The
74 observed reflections were consistent with the $P2_1/n$ space group, with a resulting discrepancy
75 factor, R_{int} , of 0.055. Structure refinements based on F^2 were performed using the ShelX program

76 (Sheldrick 2008) implemented in the WinGX system (Farrugia 2012). The atomic parameters
77 reported by Schmidt et al. (1998) were used as starting parameters and neutral scattering factors
78 (Ibers and Hamilton 1974) were employed for Si, Al and O. All atom positions were refined
79 allowing for anisotropic displacement parameters. We performed structure refinements at ambient
80 conditions with both fixed and refined occupancies for Si and Al in the two non-equivalent cation
81 sites, respectively. Within uncertainties, the two models gave identical results for atomic positions
82 and bond distances. The fully occupied model was therefore chosen for the following discussion. A
83 total of 55 parameters were refined using 1348 unique reflections with resulting discrepancy factor
84 $R1 = 0.054$. Atomic positions and displacement parameters are reported in the deposited CIF.

85

86 **High-pressure experiments**

87 The Phase Egg single-crystal was loaded in a BX90 (Kantor et al. 2012) diamond-anvil cell (DAC)
88 equipped with 350 μm culet sized diamonds. A 200 μm rhenium gasket was pre-indented to ~ 60
89 μm and a 200 μm hole was cut. Ruby spheres were added for in situ pressure determination. The
90 gas-loading system installed at BGI (Kurnosov et al. 2008) was used to load neon at 1.5 kbar
91 pressure as a pressure transmitting medium.

92 High-pressure single-crystal X-ray diffraction was performed at the Extreme Conditions Beamline
93 P02.2 at PETRA III at the Deutsches Elektronen Synchrotron (DESY). Intensity data were collected
94 at 15 pressure points between 1.09 and 23.33 GPa using a focused monochromatic 0.2907 \AA beam
95 with a beam size of 2 x 4 μm^2 and a PerkinElmer area detector calibrated using a single-crystal of
96 enstatite. Diffraction images were collected in omega scans between -34° to $+34^\circ$ in 1° steps with
97 an exposure time of 1 s. The pressure in the cell was increased using a pressure membrane and
98 measured from the ruby Raman fluorescence shift according to the calibration of Dewaele et al.
99 (2008). Data integration was performed using the CrysAlis package (Oxford Diffraction 2006).

100 More than 520 reflections were used at all but two pressure points (120 and 371 reflections at 6.92
101 and 11.67 GPa respectively) to determine the unit-cell lattice parameters reported in Table 1.
102 Structure refinements were performed at 10 different pressure points following the same procedure
103 as used for the room pressure intensity data. However, given the smaller number of unique
104 reflections due to the restrictions imposed by the use of a DAC, the oxygen sites were refined
105 isotropically. At each pressure point, the atomic positions of the previous pressure were used as
106 starting parameters for the refinement. The number of unique reflections varied between 496 and
107 687 with R_{int} between 0.0246 and 0.1902, while the total number of parameters was reduced to 36.
108 The resulting discrepancy factors, RI , ranged between 0.0405 and 0.1059. Details of the structural
109 refinements, atomic positions and displacement parameters are reported in the deposited CIF.

110

111 RESULTS AND DISCUSSION

112 **Compressibility of Phase Egg**

113 The unit-cell lattice parameters of Phase Egg are shown in Figure 2 as a function of pressure and
114 compared to literature data. No evidence for phase transitions can be observed in agreement with
115 the results reported by Vanpeteghem et al. (2003). A plot of the normalized pressure F versus the
116 Eulerian strain f (Angel 2000) indicates that a third order Birch-Murnaghan equation of state (EoS)
117 is required to fit the P - V data (Figure S1). The room pressure unit-cell volume, V_0 , the bulk
118 modulus, K_0 , and its pressure derivative, K_0' , were refined using the software EoSFit7c (Angel et al.
119 2014) resulting in the following EoS parameters: $V_0 = 214.08(17) \text{ \AA}^3$, $K_0 = 153(8) \text{ GPa}$ and $K_0' =$
120 $8.6(1.3)$ (Table 2). Note that in the fitting procedure the unit-cell volume collected at room pressure
121 was not considered in order to avoid biases due to the different techniques used (*in-house*
122 diffractometer with point detector vs. synchrotron radiation with a two-dimensional detector).
123 The V_0 obtained in this study is larger than that measured in earlier studies (Schmidt et al. 1998;
124 Vanpeteghem et al. 2003), but is in agreement with the unit-cell volume measured *in-house* at

125 ambient conditions for our sample (Figure 2A). The chemical analysis of our sample shows small
126 deficiencies of silicon and aluminum, which we assume to be substituted by hydrogen to ensure
127 charge balance. Schmidt et al. (1998) reported an Al:Si ratio close to unity and Vanpeteghem et al.
128 (2003) assumed unity based on the nominal composition of the starting material used to synthesize
129 Phase Egg. The presence of very small amounts of Al and Si vacancies in our sample, as well as the
130 different synthesis conditions (i.e. higher pressure and temperature used in this study) and the
131 different X-ray diffraction techniques used (single-crystal vs. powder diffraction) may explain the
132 difference in unit-cell volumes among the three studies. Note, however, that the room pressure
133 crystal structure refinements performed here gave identical results within uncertainties when
134 refining or fixing to unity the Al and Si occupancies. This implies that the effect of vacancies on the
135 crystal structure of Phase Egg cannot be resolved in our structural model.

136 The K_0 obtained in this study is in agreement with that reported in the high-pressure powder
137 diffraction study of Vanpeteghem et al. (2003) within uncertainties (Table 2). The pressure
138 derivative determined in this study is instead larger than that reported by Vanpeteghem et al.
139 (2003), resulting in a lower compressibility of our sample at high pressure. However, the F-f plot
140 constructed using the data reported by Vanpeteghem et al. (2003) (Fig. S2) reveals a kink at about
141 16 GPa with the lower pressure data suggesting a much steeper slope than the higher pressure data.
142 Therefore, the value of K' reported by Vanpeteghem et al. (2003) is likely an average between these
143 two clearly different compression behaviors. A change in compression mechanism is indeed
144 suggested by the high-pressure variation of the β angle which shows a rapid decrease with pressure
145 up to 16 GPa (Figure 2B) but then remains practically constant at a value of $\sim 97.8^\circ$ up to the
146 largest pressure reached both in this study and in the study of Vanpeteghem et al. (2003). This
147 change in compression behavior is clearly more pronounced in the powder data since we do not
148 observe a sharp kink in the F-f plot constructed with the data collected in this study. This is likely

149 due to the different stress states present in the powder and in the single-crystal diamond-anvil cell
150 experiments.

151 The variation with pressure of the unit-cell axes is very anisotropic as already suggested by
152 Vanpeteghem et al. (2003). As can be seen from Figure 2C, the **b** axis is the most compressible
153 direction, despite being the shortest of the three unit-cell parameters. Linearized Birch-Murnaghan
154 EoS (Angel et al. 2014) were fitted to the data (Table 2). The linear modulus for the compression
155 the **a** axis can be fitted using a second order Birch-Murnaghan EoS as the data plot on a horizontal
156 along the **b** axis is much lower than those along the other two axes (Table 2). Moreover, whereas
157 line in a F-f plot (Angle et al. 2000), both **b** and **c** axes have a very steep slope suggesting a larger
158 stiffening of the Phase Egg structure with pressure along these two directions. In order to compare
159 the axial compressibility obtained in this study with that obtained by Vanpeteghem et al. (2003), we
160 have refitted the published data using the same linearized Birch-Murnaghan EoS, since in the
161 mentioned study the axial behavior has been described using simple polynomials. Both **b** and **c** axes
162 appear to have identical M_0 within the uncertainties. However, the **a** axis of the sample investigated
163 in this study appears more compressible than that of the sample investigated by Vanpeteghem et al.
164 (2003). Moreover, the polynomial variation with pressure of the **a** axis reported in Vanpeteghem et
165 al. (2003) has a negative coefficient of the quadratic term which implies that this direction becomes
166 softer with increasing pressure. This further supports the hypothesis that the published data were
167 obtained in a different stress environment with respect to that present in our experiment. Since we
168 have not observed broadening of the single-crystal reflections up to the maximum pressure reached,
169 we expect that the condition in our study was effectively hydrostatic.

170 In crystals with orthorhombic or higher symmetry, the changes of the unit-cell lattice parameters
171 with pressure define the variation of the strain ellipsoid describing the distortion of the unstrained
172 crystal with increasing pressure (Nye 1985). However, in the case of monoclinic and triclinic

173 systems, unit-cell angles may also vary with pressure, therefore the largest and smallest lattice
174 changes in the crystal are not necessarily aligned parallel to the crystallographic axes.

175 The strain ellipsoid tensor components (Ohashi and Burnham, 1973) for Phase Egg which has a
176 monoclinic symmetry have been calculated from the unit-cell lattice parameters at each pressure
177 based on the Cartesian coordinate system with $\mathbf{X} // \mathbf{a}$ $\mathbf{Y} // \mathbf{b}$ and $\mathbf{Z} // \mathbf{c}^*$ according to the following
178 equations:

$$179 \quad e_{11} = \frac{a}{a_0} - 1 \qquad e_{22} = \frac{b}{b_0} - 1 \qquad e_{33} = \frac{c \sin \beta}{c_0 \sin \beta_0} - 1$$

$$180 \quad e_{13} = \frac{1}{2} \left(\frac{c \cos \beta}{c_0 \sin \beta_0} - \frac{a \cos \beta_0}{a_0 \sin \beta_0} \right) \qquad e_{12} = e_{23} = 0$$

181 where the zero denotes the room pressure unit-cell parameters.

182 The principal strain components ε_{11} , ε_{22} and ε_{33} and their orientation with respect to the
183 crystallographic axes have been derived by diagonalization of the symmetrical strain tensor (Table
184 3). Due to the monoclinic symmetry, ε_{22} lies parallel to the \mathbf{b} axis and has indeed the largest
185 absolute values at all pressures indicating that this is the most compressible direction. The principal
186 strain components ε_{11} and ε_{33} lie on the \mathbf{a} - \mathbf{c} plane, the former being the stiffer direction at $\sim 30^\circ(2)$
187 from \mathbf{a} toward \mathbf{c} . This direction is approximately perpendicular to the plane (9 0 4) and represents
188 the direction along which columns of octahedra extend, having their shared edge perpendicular to
189 this direction. The value of the unit strain (Hazen et al. 2000) in the stiffest direction, i.e. its
190 fractional change per GPa remains invariant with pressure (Table 3), whereas the unit strain values
191 in the other two directions, and especially that along the \mathbf{b} axis, steadily decrease with pressure,
192 implying that their compression significantly contribute to the pressure derivative of the bulk
193 modulus. The orientation of the strain ellipsoid does not vary over the pressure range investigated in
194 this study.

195

196 **High-pressure Structure**

197 The individual octahedral bond distances for Si and Al are shown in Figure 3. At ambient pressures,
198 the Si-O bond lengths are generally between 1.75 and 1.8 Å, with the exception of the Si-O4 bond
199 that shows a value of about 2 Å in agreement with the study of Schmidt et al. (1998). At lower
200 pressures, the coordination number of the silicon atom is therefore better described by 5 + 1.
201 A rapid reduction of the bond distance between the Si and the O4 atoms with pressure is clearly
202 visible in Figure 3. The reduction between ambient conditions and the highest pressure point at 23.3
203 GPa is more than 9%, where the majority of this reduction has been already reached at ~ 16 GPa.
204 Above this pressure, the Si octahedral coordination is much more regular and the Si-O4 bond
205 becomes as stiff as the other Si-O bond distances (Figure 3). The Si-O4 bond contributes mainly to
206 the compressions of the **b** and **c** axis. The stiffest Si-O bond is the Si-O3 which does not show any
207 significant compression. All other Si octahedral bonds have similar compression rates and their
208 bond distances reduce by ~1.5 – 2% up to the highest pressure measured.
209 The compression of the Al octahedron is more uniform when compared to the Si octahedron, with
210 two Al-O4 and one Al-O2 bond distances showing similar compressibilities, i.e. bond distance
211 reductions between 3.7 and 4.4 % in the studied pressure range. The Al-O1 bond distance decreases
212 by ~ 2.3% and one of the Al-O3 bond distances reduces by ~ 1.4% between room pressure and 23.3
213 GPa. The other Al-O3 bond distance shows practically no compression, since the O3 atom connects
214 the Si and the Al octahedron and forms the stiffest Si-O3 bond (Fig. 3).
215 The analysis of O-O distances reveals a more complicated compression mechanism than the simple
216 picture suggested by Vanpeteghem et al. (2003). These authors indicated as a possible explanation
217 for the large compressibility of the **b** axis the fact that the largest O-O distance lies in a direction
218 nearly parallel to this axis as opposed to shorter O-O distances which are nearly parallel to the **a** and
219 **c** directions. This reasoning is based on the assumption that longer distances are more compressible
220 than shorter ones. However, this appears to be an invalid assumption in the case of Phase Egg,
221 where the O-O distances involving the O4 atoms are most compressible independently from their

222 value and direction. This is likely a consequence of the major compression of the Si-O4 bond. For
223 example, the O4-O1 and O4-O2 distances which are perpendicular to the **b** direction (and therefore
224 do not contribute to its compressibility) are relatively short but decrease by more than 4% in the
225 pressure range investigated (Figure 4), whereas the longer distance indicated by Vanpeteghem et al.
226 (2003), which correspond in our study to the O4-O4 distance and contributes to the compressibility
227 of the **b** direction, decreases only by ~ 3.8% (Figure 4). As expected, the distances between the
228 oxygen belonging to the shared octahedral edges are the least compressible and decrease less than
229 1% in the pressure range investigated, except for the O3-O4 shared edge which undergoes a 3.3%
230 reduction between room pressure and 23.3 GPa (Figure 4). Only two O-O distances show a major
231 compressibility, e.g. the O3-O3 distance between the columns of Al octahedra across the voids
232 (Figure 1B). This distance which lies parallel to the **b** direction decreases by more than 9% up to
233 23.3 GPa (Figure 4) and is therefore responsible for the large compressibility of this axis.

234

235

IMPLICATIONS

236 Phase Egg is a member of the Al₂O₃-SiO₂-H₂O system. In contrast to the Mg-Si endmember, the
237 phases in the aluminum system are stable at temperatures of a typical mantle geotherm (Fukuyama
238 et al. 2017). Phase Egg and several other phases are therefore good candidates for water transport
239 into the Earth's deep mantle through subduction of sediments and oceanic crust. Direct evidence for
240 the occurrence of Phase Egg in the Earth's mantle comes from the chemical composition of a
241 diamond inclusion that showed a 1:1 Al to Si ratio and was assigned to Phase Egg (Wirth et al.
242 2007).

243 The most prominent feature in the high-pressure behavior of Phase Egg is the change in
244 compression behavior of the Si-O4 bond in the Si-octahedron. Computational studies on the δ -
245 AlOOH structure suggest that the compressibility of the structure is related to hydrogen bonding
246 symmetrization (Tsuchiya et al. 2002). Based on this, Vanpeteghem et al. (2003) suggested that a

247 stiffening of the H-O bonds could explain the curvature of the pressure dependence of the *b*-lattice
248 parameter observed at high pressure for Phase Egg.
249 Schmidt et al. 1998 reported a position for the hydrogen atom that suggests an asymmetric O4-
250 H...O3 configuration over the void space. Symmetrization and strengthening of similar
251 configurations with increasing pressure were reported from computational calculations for diaspore
252 (Friedrich et al. 2007) as well as from computational and experimental studies for iron
253 oxyhydroxide (Xu et al. 2013). In diaspore the symmetrization of the hydrogen bonding and a high
254 compressibility along the void space is related to a strong compression of the donor-acceptor
255 distance with increasing pressure. In Phase Egg the O3...O4 distance decreases from 2.608(1) Å at
256 ambient pressure to 2.516(3) Å at 23.3 GPa. This represents a reduction of only 3.5% much smaller
257 for example than the O3...O3 distance over the void space which reduces by about 9% in the same
258 pressure range (Figure 4). From our results, therefore, there is no evidence of symmetrization of the
259 O4-H...O3 configuration in the pressure range where Phase Egg may be stable in the Earth's
260 mantle. The Si-O4 bond distance is rapidly decreasing until 16 GPa pressure, strengthening the
261 bond and weakening the O4-H bond. Thus, it is more likely that the regularization and further
262 stiffening of the silicon octahedron is the reason for the change in compressional behavior above 16
263 GPa. Moreover, the high stability field to pressures and temperatures of the upper lower mantle of
264 Phase Egg (Pamato et al. 2015) may be due to the decreasing distortion of the Si-octahedron which
265 reaches a regular 6-fold.

266

267

ACKNOWLEDGMENT

268 This research was supported through the project "GeoMaX" funded under the Emmy-Noether
269 Program of the German Science Foundation (MA4534/3-1).

270

271 **References**

- Angel, R. J.; (2000) Equation of State. *Reviews in Mineralogy and Geochemistry*, 41, 35-59
- Angel, R.J., and Finger, L.W. (2011) SINGLE: a program to control single-crystal diffractometers. *Journal of Applied Crystallography*, 44, 247–251.
- Angel, R. J., Alvaro, M., Gonzales-Platas, J. (2014) EosFit7c and a Fortran module (library) for equation of state calculations. *Zeitschrift für Kristallographie*.
- Deweale, A., Torrent, M., Loubeyre, P., Mezouar M. (2008) Compression curves of transition metals in the Mbar range: Experiments and projector augmented-wave calculations. *Physical Review B*, 78, 104102
- Eggleton, R.A., Boland, J.N., and Ringwood, A.E. (1978) High pressure synthesis of a new aluminium silicate: $\text{Al}_5\text{Si}_5\text{O}_{17}(\text{OH})$. *Geochemical Journal*, 12, 191–194.
- Farrugia, L.J. (2012) WinGX and ORTEP for Windows: an update. *Journal of Applied Crystallography*, 45, 849–854.
- Fukuyama, K., Ohtani, E., Shibasaki, Y., Kagi, H., and Suzuki, A. (2017) Stability field of phase Egg, AlSiO_3OH at high pressure and high temperature: possible water reservoir in mantle transition zone. *Journal of Mineralogical and Petrological Sciences*, 112, 31–35.
- 272 Friedrich, A., Wilson, D. J., Haussühl, E., Winkler, B., Morgenroth W., Refson, K., and Milman, V.
273 (2007) High-pressure properties of diaspore, $\text{AlO}(\text{OH})$. *Physics and Chemistry of Minerals*,
274 34, 145-157.
275
- Gatta, G.D., Morgenroth, W., Dera, P., Petitgirard, S., and Liermann, H.-P. (2014) Elastic behavior and pressure-induced structure evolution of topaz up to 45 GPa. *Physics and Chemistry of Minerals*, 41, 569–577.
- Hazen, R.M., Downs, R.T., and Prewitt, C.T. (2000) Principle of comparative crystal chemistry. *Reviews in Mineralogy and Geochemistry*, 41, 1-33.
- Kantor, I., Prakapenka, V., Kantor, A., Dera, P., Kurnosov, A., Sinogeikin, S., Dubrovinskaia, N., and Dubrovinsky, L. (2012) BX90: A new diamond anvil cell design for X-ray diffraction and optical measurements. *Review of Scientific Instruments*, 83, 125102.
- King, H.E., and Finger, L.W. (1979) Diffracted beam crystal centering and its application to high-pressure crystallography. *Journal of Applied Crystallography*, 12, 374–378.
- Kurnosov, A., Kantor, I., Boffa-Ballaran, T., Lindhardt, S., Dubrovinsky, L., Kuznetsov, A., and Zehnder, B.H. (2008) A novel gas-loading system for mechanically closing of various types of diamond anvil cells. *Review of Scientific Instruments*, 79, 045110.
- Ibers, J. A. and Hamilton, W. C. (1974) *International tables for X-ray crystallography*, Vol. IV, Kynoch, Birmingham, UK
- Nye, J.F. (1985) *Physical Properties of Crystals: Their Representation by Tensors and Matrices*, 352 p. Oxford University Press, Oxford, New York.
- Ohashi, Y., and Burnham, C.W. (1973) Clinopyroxene lattice deformations: The role of chemical substitution and temperature. *American Mineralogist*, 58, 843-849.

- Pamato, M.G., Myhill, R., Boffa Ballaran, T., Frost, D.J., Heidelbach, F., and Miyajima, N. (2015) Lower-mantle water reservoir implied by the extreme stability of a hydrous aluminosilicate. *Nature Geoscience*, 8, 75–79.
- Sano, A., Ohtani, E., Kubo, T., and Funakoshi, K. (2004) In situ X-ray observation of decomposition of hydrous aluminum silicate AlSiO_3OH and aluminum oxide hydroxide $\delta\text{-AlOOH}$ at high pressure and temperature. *Journal of Physics and Chemistry of Solids*, 65, 1547–1554.
- Schmidt, M.W., Finger, L.W., Angel, R.J., and Dinnebier, R.E. (1998) Synthesis, crystal structure, and phase relations of AlSiO_3OH , a high-pressure hydrous phase. *American Mineralogist*, 83, 881–888.
- Sheldrick, G.M. (2008) A short history of SHELX. *Acta Crystallographica Section A: Foundations of Crystallography*, 64, 112–122.
- Tsuchiya, J., Tsuchiya, T., Tsuneyuki, S., and Yamanaka, T. (2002) First principles calculation of a high-pressure hydrous phase, $\delta\text{-AlOOH}$. *Geophysical Research Letters*, 29, 1909.
- Vanpeteghem, C.B., Ohtani, E., Kondo, T., Takemura, K., and Kikegawa, T. (2003) Compressibility of phase Egg AlSiO_3OH : Equation of state and role of water at high pressure. *American Mineralogist*, 88, 1408–1411.
- Wirth, R., Vollmer, C., Brenker, F., Matsyuk, S., and Kaminsky, F. (2007) Inclusions of nanocrystalline hydrous aluminium silicate “Phase Egg” in superdeep diamonds from Juina (Mato Grosso State, Brazil). *Earth and Planetary Science Letters*, 259, 384–399.
- Xue, X., Kanzaki, M., Fukui, H., Ito, E., and Hashimoto, T. (2006) Cation order and hydrogen bonding of high-pressure phases in the $\text{Al}_2\text{O}_3\text{-SiO}_2\text{-H}_2\text{O}$ system: An NMR and Raman study. *American Mineralogist*, 91, 850–861.

276 Xu, W., Greenberg, E., Rozenberg, G. K., Pasternak, M. P., Bykova, E., Boffa-Ballaran, T.,
277 Dubrovinsky, L., Prakapenka, V., Hanfland, M., Vekilova, O. Y., Simak, S. I. and
278 Abrikosov, I. A. (2013) Pressure-Induced Hydrogen Bond Symmetrization in Iron
279 Oxyhydroxide. *Physical Review Letters*, 111, 175501.

280

281

Captions

282 **Figure 1.** The structure of Phase Egg in the (010) and (100) plane. Silicon octahedra are shown in
283 dark blue and aluminum octahedra are light blue. The oxygen atoms are marked red and labeled
284 according to the nomenclature presented by Schmidt et al. (1998). The hydrogen atom (purple)
285 positions are taken from Schmidt et al. (1998) and are situated in the empty channels.

286

287 **Figure 2.** (A) Unit-cell volume, (B) β angle and (C) relative unit-cell lattice parameters (a/a_0 , b/b_0
288 and c/c_0) of Phase Egg. Open circles represent the room pressure data measured in this study,
289 whereas filled circles are results from the high-pressure measurements. The solid curves represent
290 the third-order Birch-Murnaghan Equation of State fit. Literature data are shown for comparison
291 (Vanpeteghem et al. 2003, Schmidt et al. 1998 and Xue et al. 2006). Uncertainties are smaller or
292 comparable to the symbol size unless error bars are shown.

293

294 **Figure 3.** (A) Si-O individual bond distances. The Si-O4 bond is elongated at room pressure and is
295 more compressible than all the other bonds. At pressures above 16 GPa the silicon octahedron
296 adopts a more regular shape and becomes stiffer. (B) Al-O individual bond distances. Open circles
297 represent room pressure data measured in this study, whereas filled circles are the high-pressure
298 results from this study. Uncertainties are smaller or comparable to the symbol size.

299

300 **Figure 4.** Selected oxygen–oxygen distances. The O3-O3 bond distance is measured across the
301 voids between two columns of Al octahedra and shows the strongest reduction with pressure of all
302 O-O distances. Squared symbols represent bonds involving octahedral shared edges. Open symbols
303 represent room pressure data measured in this study, whereas filled symbols are the high-pressure
304 results from this study. Uncertainties are smaller or comparable to the symbol size.

305

306

307 **Figure S1.** Eulerian finite strain, f , vs. normalized pressure, F , constructed using the V_0 obtained
308 from the equation of state fit. The solid line is the weighted linear fit through the data, its steep
309 slope indicates a $K' > 4$.

310

311 **Figure S2.** Eulerian finite strain, f , vs. normalized pressure, F , constructed using the data reported
312 in Vanpeteghen et al. (2003). The solid line is the fit using the EoS parameters reported in the
313 mentioned study. A change of compression behavior is apparent at about 16 GPa.

314

315

316

317

318 **TABLE 1.** Unit-cell lattice parameters and volumes of Phase Egg collected at different pressures.

319 Numbers in brackets refer to the uncertainty in the last given digit.

	Pressure	a	b	c	Volume	β
	[GPa]	[Å]	[Å]	[Å]	[Å ³]	[°]
320	0.0001*	7.1835(2)	4.3287(2)	6.9672(2)	214.43(1)	98.201(2)
321						
322	1.09(5)	7.1738(2)	4.3092(4)	6.9499(3)	212.69(2)	98.114(4)
	1.82(5)	7.1666(2)	4.2977(3)	6.9375(2)	211.553(17)	98.080(3)
323	3.09(7)	7.1613(3)	4.2819(4)	6.9249(3)	210.28(2)	98.007(5)
	4.15(8)	7.1505(4)	4.2632(7)	6.9107(5)	208.64(4)	97.953(8)
324	4.87(6)	7.1488(4)	4.2564(5)	6.9071(6)	208.14(3)	97.966(9)
	6.92(9)	7.1267(4)	4.2357(5)	6.8801(6)	205.74(3)	97.853(9)
325	9.74(10)	7.1128(3)	4.2132(3)	6.8639(4)	203.78(2)	97.838(6)
	11.67(9)	7.0951(6)	4.1968(6)	6.8456(7)	201.93(4)	97.842(11)
326	14.54(11)	7.0693(2)	4.1722(2)	6.8187(2)	199.252(12)	97.805(3)
	16.82(11)	7.0533(2)	4.1583(2)	6.8029(3)	197.687(14)	97.793(4)
327	17.27(15)	7.0529(2)	4.1561(3)	6.8030(3)	197.567(17)	97.800(5)
	18.56(13)	7.0424(4)	4.1452(4)	6.7950(5)	196.52(3)	97.814(8)
328	19.33(17)	7.0356(3)	4.1403(3)	6.7875(4)	195.886(19)	97.806(6)
	21.44(18)	7.0263(3)	4.1302(4)	6.7774(5)	194.86(3)	97.799(8)
329	23.33(18)	7.0138(3)	4.1209(3)	6.7661(4)	193.75(2)	97.802(6)

330 * measured using the Huber diffractometer at BGI

331

332

333

334

335

336

337

338

339

340

341

342 **TABLE 2.** EoS parameters resulting from Birch-Murnaghan equation of state fits for both bulk and
 343 axial compressibilities of Phase Egg. The axial compressibilities from a previous powder diffraction
 344 experiment (Vanpeteghem et al. 2003) have been recalculated in this study. Numbers in brackets
 345 refer to the uncertainty in the last given digit.

	Vanpeteghem et al. (2003)		This study
	published	refitted	
V_0 (Å ³)		211.41 (11)	214.08 (17)
K_0 (GPa)	157 (4)	155 (5)	153 (8)
K'	6.5 (4)	6.7 (5)	8.6 (1.2)
a_0 (Å)		7.136 (6)	7.1848 (12)
M_{a0} (GPa)		942 (58)	833 (14)
M'_a		12*	12*
b_0 (Å)		4.322 (5)	4.327 (2)
M_{b0} (GPa)		226 (21)	240 (16)
M'_b		25 (3)	30 (3)
c_0 (Å)		6.930 (5)	6.963 (2)
M_{c0} (GPa)		498 (57)	497 (40)
M'_c		32 (7)	36 (7)

346 * Second-order Birch-Murnaghan EoS
 347
 348

349

350

351 **TABLE 3.** Principal strain components, their orientation with respect to the crystallographic axes
 352 and the resulting unit strain components for the strain ellipsoid of Phase Egg. Numbers in brackets
 353 refer to the uncertainty in the last given digit.

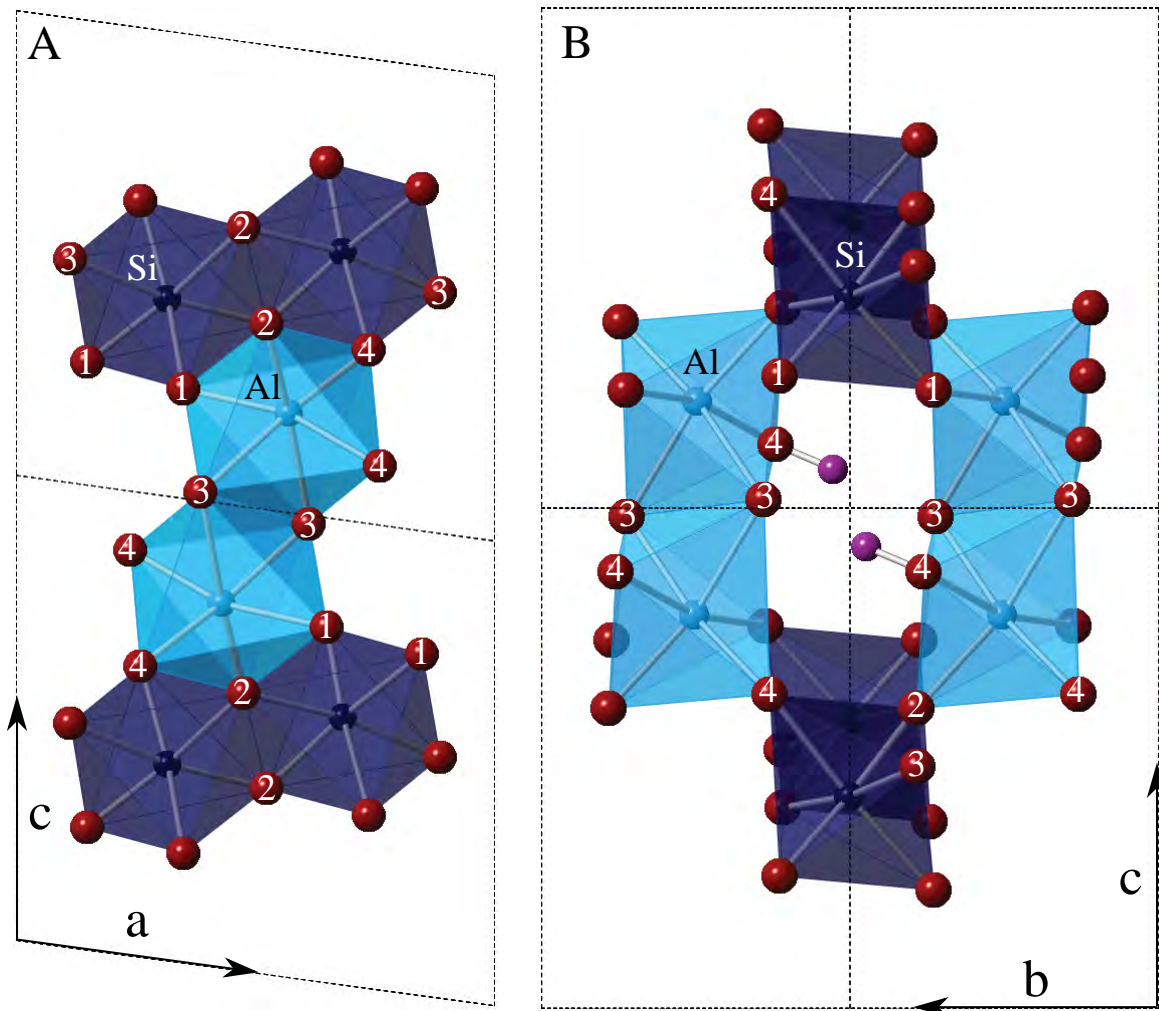
P (GPa)	$\epsilon_{11} 10^{-3}$	$\epsilon_{22} 10^{-3}$	$\epsilon_{33} 10^{-3}$	$\epsilon_{11} \wedge \mathbf{a}$ ($^{\circ}$)*	ϵ_{11}/GPa 10^{-3}	ϵ_{22}/GPa 10^{-3}	ϵ_{33}/GPa 10^{-3}
1.09(5)	-0.85 (8)	-4.50 (10)	-2.76 (8)	30.7	-0.78	-4.13	-2.54
1.82(5)	-1.71 (7)	-7.16 (8)	-4.59 (7)	28.0	-0.94	-3.93	-2.52
3.09(5)	-2.07 (8)	-10.81 (10)	-6.61 (8)	28.4	-0.67	-3.50	-2.14
4.15(5)	-3.24 (9)	-15.13 (17)	-8.85 (9)	29.5	-0.78	-3.65	-2.13
4.87(5)	-3.63 (9)	-16.70 (12)	-9.25 (10)	27.6	-0.74	-3.43	-1.90
6.92(5)	-5.96 (9)	-21.48 (12)	-13.61 (10)	30.4	-0.86	-3.10	-1.97
9.74(5)	-7.85 (8)	-26.68 (8)	-15.94 (9)	29.8	-0.81	-2.74	-1.64
11.67(5)	-10.39 (10)	-30.47 (15)	-18.51 (11)	29.1	-0.89	-2.61	-1.59
14.54(5)	-13.74 (7)	-36.16 (6)	-22.51 (8)	29.7	-0.94	-2.49	-1.55
16.82(5)	-15.89 (7)	-39.37 (6)	-24.83 (8)	30.0	-0.94	-2.34	-1.48
17.27(5)	-15.99 (7)	-39.87 (8)	-24.80 (8)	30.0	-0.93	-2.31	-1.44
18.56(5)	-17.51 (9)	-42.39 (10)	-25.92 (9)	30.3	-0.94	-2.28	-1.40
19.33(5)	-18.42 (8)	-43.52 (8)	-27.02 (9)	30.2	-0.95	-2.25	-1.40
21.44(5)	-19.69 (8)	-45.86 (10)	-28.47 (9)	30.0	-0.92	-2.14	-1.33
23.33(5)	-21.44 (8)	-48.01 (8)	-30.09(9)	30.2	-0.92	-2.06	-1.29

354
 355 * Angle between ϵ_{11} and \mathbf{a} toward \mathbf{c} .
 356

357

358

Figure 1



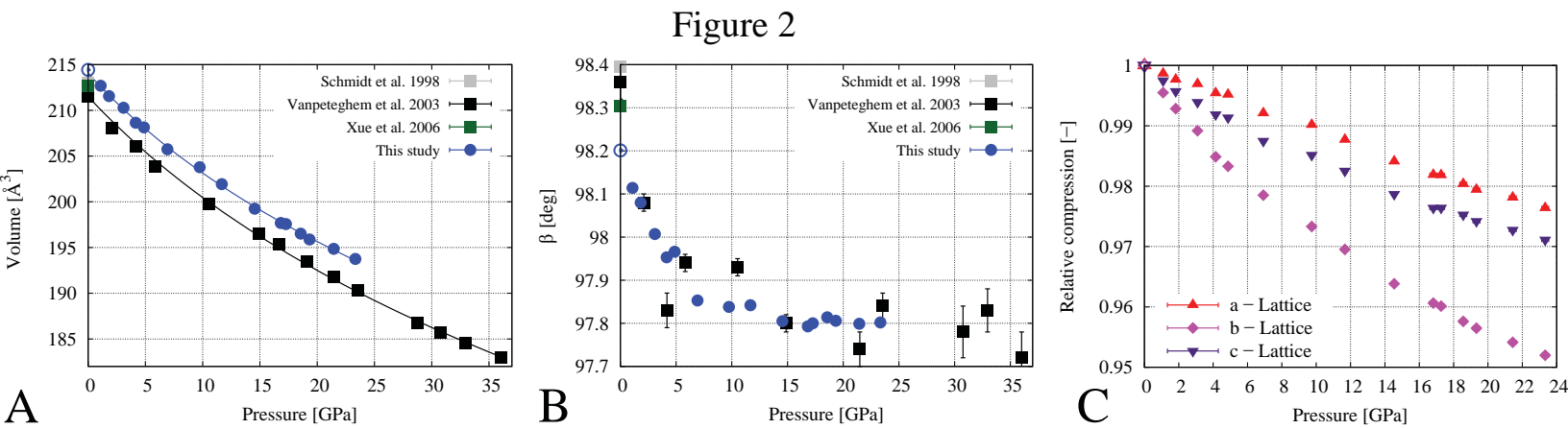


Figure 3

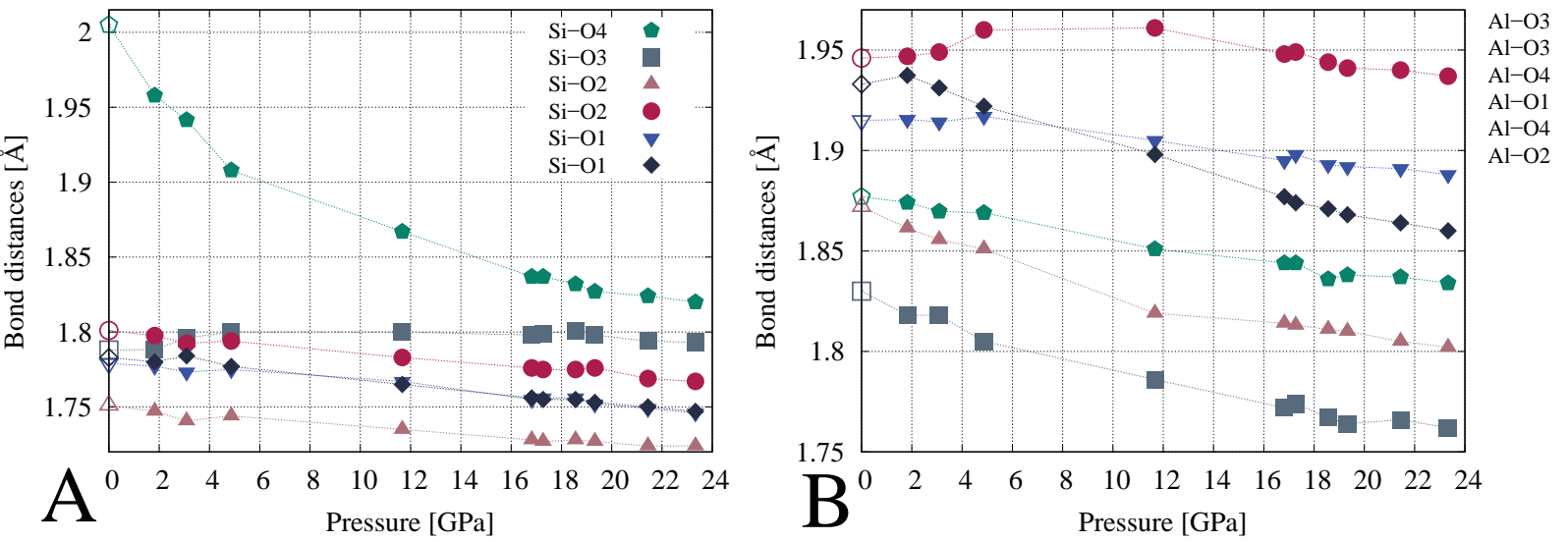


Figure 4

